Heterometallic Ru–Pt metallacycle for two-photon photodynamic therapy

Zhixuan Zhou[a,1], Jiangping Liu[b,1], Thomas W. Rees[b], Heng Wang[c], Xiaopeng Li[c], Hui Chao[b,2], and Peter J. Stang[a,2]

[a]Department of Chemistry, University of Utah, Salt Lake City, UT 84112; [b]MOE Key Laboratory of Bioinorganic and Synthetic Chemistry, School of Chemistry, Sun Yat-sen University, 510275 Guangzhou, People's Republic of China; and [c]Department of Chemistry, University of South Florida, Tampa, FL 33620

Contributed by Peter J. Stang, April 22, 2018 (sent for review February 2, 2018; reviewed by Chad A. Mirkin and Melanie S. Sanford)

As an effective and noninvasive treatment of various diseases, photodynamic therapy (PTD) relies on the combination of light, a photosensitizer, and oxygen to generate cytotoxic reactive oxygen species that can damage malignant tissue. Much attention has been paid to covalent modifications of the photosensitizers to improve their photophysical properties and to optimize the pathway of the photosensitizers interacting with cells within the target tissue. Herein we report the design and synthesis of a supramolecular heterometallic Ru–Pt metallacycle via coordination-driven self-assembly. While inheriting the excellent photostability and two-photon absorption characteristics of the Ru(II) polypyridyl precursor, the metallacycle also exhibits red-shifted luminescence to the near-infrared region, a larger two-photon absorption cross-section, and higher singlet oxygen generation efficiency, making it an excellent candidate as a photosensitizer for PTD. Cellular studies reveal that the metallacycle selectively accumulates in mitochondria and nuclei upon internalization. As a result, singlet oxygen generated by photoexcitation of the metallacycle can efficiently trigger cell death via the simultaneous damage to mitochondrial function and intranuclear DNA. In vivo studies on tumor-bearing mice show that the metallacycle can efficiently inhibit tumor growth under a low light dose with minimal side effects. The supramolecular approach presented in this work provides a paradigm for the development of PDT agents with high efficacy.

supramolecular coordination complex | two-photon absorption | photodynamic therapy | mitochondria | nucleus

Noncovalent interactions are widely employed in natural systems for the construction of complex and functional biomolecules that perform various biological processes. Inspired by nature, chemists utilize dative metal–ligand bonds between Lewis basic organic donors and Lewis acidic metal acceptors to guide the organization of molecular precursors. Due to the good directionality and reversibility of metal–ligand coordination interaction, various discrete supramolecular coordination complexes (SCCs) with well-defined sizes and shapes have been rationally designed and synthesized in high efficiency via coordination-driven self-assembly (1–3). New functionalities that are not observed in an individual precursor may arise from the formation of SCC systems. For example, SCCs can accommodate guest molecules (4–6) or catalyze reactions (7, 8) due to the formation of large inner cavities. Highly emissive SCCs can be obtained by restricting the intramolecular motions of fluorophores with aggregation-induced emission character within the rigid framework (9). The macrocyclic structure of SCCs can enhance their cellular uptake compared with their corresponding small-molecule precursor and allow binding to biomolecules with high affinity (10–12).

Photodynamic therapy (PDT) is a medical procedure that requires a combination of a photosensitizer and light in an oxygenated environment (13, 14). Reactive oxygen species (ROS) are generated through excited-state energy transfer from a light-excited photosensitizer to oxygen and other molecules in the tissue, which induces cellular and tissue damage. PDT can induce localized damage to malignant tissues via local exposure to light, resulting in significantly reduced side effects to healthy tissues relative to traditional chemotherapy and radiotherapy. As a result, PDT has been adopted to treat a range of cancers, infections, and skin diseases in recent years (13, 14). Ru(II) complexes are an emerging class of photosensitizers featuring good water solubility, good photostability, and facile synthetic tunability (14, 15). Moreover, some Ru(II) polypyridyl complexes exhibit two-photon absorption (TPA) properties (14–16). Compared with one-photon photosensitizers, two-photon photosensitizers provide red-shifted, lower-energy wavelengths for therapeutic activation, which results in less damage to healthy tissue, enhanced spatial resolution, and a significant increase in penetration depth (14, 15). In recent years, considerable effort has been devoted to modifying the auxiliary ligands to obtain Ru(II) polypyridyl complexes with the desired photophysical and biological properties for PDT (stability, cellular uptake, subcellular distribution, and toxicity) (14, 15, 17, 18).

Combining the attractive properties of Ru(II) polypyridyl complexes with the versatility of coordination-driven self-assembly, we designed a heterometallic Ru–Pt metallacycle as a two-photon PDT agent. The incorporation of an Ru(II) polypyridyl complex into a Pt(II)-based SCC would result in several improvements. First, Pt(II) may endow the ensemble with favorable photophysical properties for biomedical applications, such as red-shifted emission and enhanced TPA activities compared with analogous small molecules (19, 20). Second, as a heavy atom, the Pt would also promote intersystem crossing, which results in more efficient ROS generation (21, 22). Third, the rigid, planar macrocyclic structure of **1** may

Significance

Photodynamic therapy is a noninvasive medical procedure in which malignant tissue is damaged by reactive oxygen species generated from targeted light irradiation on a photosensitizer. Herein, we incorporate an Ru(II)-based two-photon photosensitizer into a macrocyclic structure via coordination-driven self-assembly. Properties favorable for photodynamic therapy arise upon formation of the metallacycle, including near-infrared luminescence, strong two-photon absorption, high reactive oxygen species generation efficiency, and selective accumulation in mitochondria and nucleus that are hypersensitive to reactive oxygen species, resulting in good photodynamic therapy efficacy in both in vitro and in vivo investigations. This study shows that supramolecular coordination complexes provide a platform for efficient tuning on the photophysical and biological properties of molecules with biomedical interest.

Author contributions: Z.Z., J.L., H.C., and P.J.S. designed research; Z.Z. and J.L. performed research; H.W. and X.L. contributed new reagents or analytic tools; Z.Z., J.L., T.W.R., H.C., and P.J.S. analyzed data; and Z.Z., J.L., T.W.R., H.C., and P.J.S. wrote the paper.

Reviewers: C.A.M., Northwestern University; and M.S.S., University of Michigan.

The authors declare no conflict of interest.

[1]Z.Z. and J.L. contributed equally to this work.

[2]To whom correspondence may be addressed. Email: ceschh@mail.sysu.edu.cn or stang@chem.utah.edu.

This article contains supporting information online at www.pnas.org/lookup/suppl/doi:10.1073/pnas.1802012115/-/DCSupplemental.

Published online May 14, 2018.

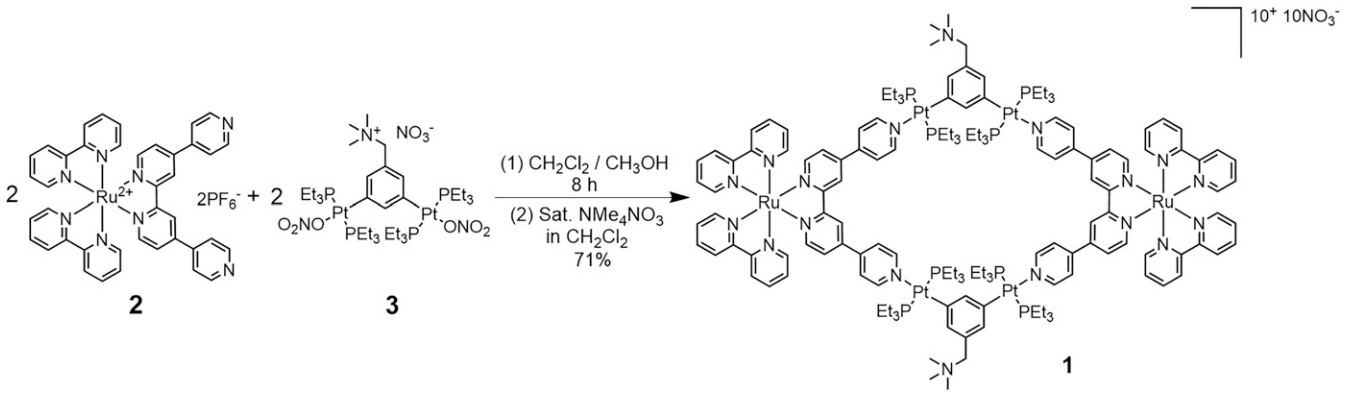

Fig. 1. Synthesis of heterometallic Ru–Pt metallacycle **1**.

be beneficial for increasing the TPA behavior due to the enhanced strain-induced charge polarization of the Ru(II) polypyridyl donor **2** (23). Finally, the highly charged nature of the resultant SCC may facilitate its internalization (10) and selective accumulation in subcellular organelles that are hypersensitive to PDT-mediated damage, such as mitochondria (16, 24) and nuclei (25). Based on this design, a heterometallic Ru–Pt metallacycle **1** was synthesized via coordination-driven self-assembly between a Ru(II) polypyridyl donor **2** and a tetramethylammonium-decorated Pt(II) acceptor **3**, as shown in Fig. 1. We investigated the photophysical properties, singlet oxygen quantum yield, cellular uptake, and intracellular localization of **1**. In vitro and in vivo studies on two-photon PDT efficacy were then conducted, which demonstrate that **1** is a potent two-photon PDT agent with low side effects.

Results and Discussion

Synthesis and Characterization of the Metallacycle. The synthesis of the heterometallic Ru–Pt metallacycle **1** is depicted in Fig. 1. Mixing equimolar amounts of Ru(II) 4,4′:2′,2″:4″,4‴-quaterpyridine (qpy) complex **2** and bis(phosphine) Pt(II) acceptor **3** resulted in the formation of a [2 + 2] metallacycle. Counterion exchange was then conducted by addition of a saturated solution of tetramethylammonium nitrate in dichloromethane to the reaction mixture to afford **1** as a deep-red solid. The product **1** was characterized by multinuclear NMR (^{1}H, ^{31}P) and electrospray ionization time-of-flight MS. The ^{31}P{^{1}H} NMR spectrum of **1** shows a sharp singlet at 13.38 ppm with concomitant ^{195}Pt satellites ($^{1}J_{Pt\text{-}P}$ = 2,647.5 Hz) (*SI Appendix*, Fig. S14), indicative of the formation of a discrete, highly symmetric metallacycle. In the mass spectrum of **1**, three peaks corresponding to the intact metallacycle with the loss of nitrate anions are observed at *m/z* = 1,301.28, 960.36, and 756.05, consistent with $[\mathbf{1}{-}3NO_3]^{3+}$, $[\mathbf{1}{-}4NO_3]^{4+}$, and $[\mathbf{1}{-}5NO_3]^{5+}$, respectively (*SI Appendix*, Fig. S15). The peaks were isotopically resolved and in good agreement with theoretical distributions, which confirmed the stoichiometry of the formation of **1**.

Photophysical Properties of the Metallacycle. The electronic absorption and emission spectra of the metallacycle **1** were recorded in nondeoxygenated aqueous solution (Fig. 2*A* and *SI Appendix*, Fig. S16). Several absorption bands are observed in the UV-visible (UV-Vis) region. The strong absorption band centered at 488 nm is attributed to a d(RuII) → π*(qpy) metal-to-ligand charge transfer transition (14, 15). The emission spectra of **1** exhibit a nonstructured band centered at 696 nm, which is red-shifted compared with the donor **2** (*SI Appendix*, Fig. S17) by 30 nm due to the stabilization of the π* orbitals of the qpy ligand upon complexation with the Pt(II) acceptor (19). Similar to other Ru(II) polypyridyl complexes (15), a large Stokes shift of 208 nm is observed for **1**. The luminescence quantum yield of **1** was determined to be 2.8% in aerated methanol solution, and the luminescence lifetime for **1** is 319 ns, indicating the phosphorescence nature of the emission. These two values are comparable to other Ru(II) polypyridyl complexes (14, 15). The near-infrared emission and long luminescence lifetime of **1** allow for ready characterization of its cellular uptake and intracellular distribution properties with less damage to healthy tissues, less scattering interference, and low autofluorescence background.

The TPA efficiency of **1** is quantified by the TPA cross-section (σ_2), which was measured in methanol from 780 to 880 nm at 10-nm intervals. The results are shown in Fig. 2*B*. The largest TPA cross-section was found to be around 800 nm with a σ_2 value of 1,371 GM. This value is much higher than $[Ru(bpy)_3]^{2+}$ (σ_2 = 66 GM) and free donor **2** (σ_2 = 83 GM) (20), as well as tetraphenylporphyrin (σ_2 = 2.2 GM) (26), a clinical photosensitizer

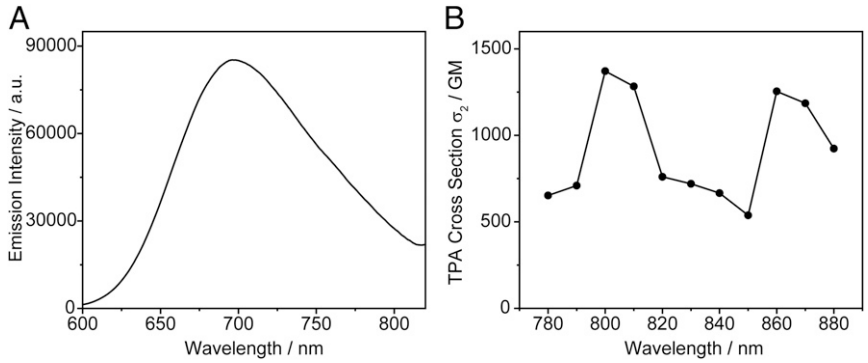

Fig. 2. Photophyscial properties of metallacycle **1**. (*A*) Emission spectrum of **1**. (*B*) Two-photon absorption cross-sections of **1** at different excitation wavelengths from 780 to 880 nm.

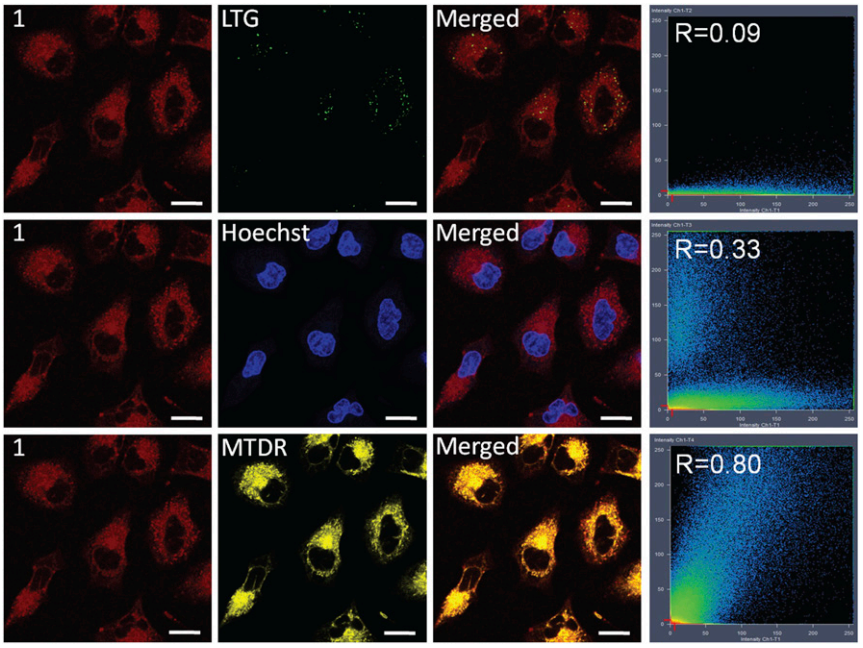

Fig. 3. Colocalization images of **1** with LTG, Hoechst, and MTDR with corresponding correlation coefficients. (Scale bars: 20 μm.)

and many two-photon bioactive organometallic compounds reported recently (14, 15, 23, 27). The increase in TPA activity is attributed to the extension of the molecular orbital of Ru(II) donor **2** onto the Pt metal center upon self-assembly (19, 20) and rigidification of the Ru(II) donor **2** upon formation of the macrocyclic structure that enhances its polarization (23). Using an excitation wavelength of 800 nm, the two-photon-induced emission spectrum of **1** was recorded, which showed similar features to the linear spectra (*SI Appendix*, Fig. S18). The two-photon-induced luminescence intensity of **1** displays quadratic dependence on the excitation power, as depicted by the logarithmic figure in *SI Appendix*, Fig. S18, *Inset*. The slope of the logarithmic plot is ∼2, confirming that the metallacycle **1** is two-photon-active.

The photostability of **1** was examined by monitoring the UV-Vis absorption spectrum of its aqueous solution under continuous light irradiation for 20 min. No significant change was observed in the absorption properties of **1** throughout the experiment (*SI Appendix*, Fig. S19), indicating excellent photostability.

Singlet Oxygen ($^1O_2$) Quantum Yield (Φ_Δ). Electron spin resonance (ESR) spectroscopy was employed to investigate the type of ROS produced by **1** upon light irradiation; 2,2,6,6-tetramethylpiperidine and 5,5-dimethyl-1-pyrroline *N*-oxide were used to detect the formation of singlet oxygen ($^1O_2$) and ·OH radical, respectively. A characteristic $^1O_2$-induced triplet signal was observed in the ESR spectrum upon exposure to 450-nm light irradiation (*SI Appendix*, Fig. S20). The intensity of the signal increased with continuous illumination. In contrast, no signals corresponding to ·OH radical formation were found. This study confirms that **1** generates $^1O_2$ upon light irradiation, analogous to many clinically applied PDT agents.

The $^1O_2$ quantum yield (Φ_Δ) is a crucial parameter for evaluating the ability of a photosensitizer to generate $^1O_2$. The Φ_Δ of **1** was assessed by directly measuring the luminescence of $^1O_2$ at 1,270 nm following photoexcitation and compared with $[Ru(bpy)_3]^{2+}$ (Φ_Δ = 81%) (*SI Appendix*, Fig. S21). The Φ_Δ of **1** was determined to be 89%. Also, indirect Φ_Δ assay was conducted using 1,3-diphenyl-isobenzofuran (DPBF) as $^1O_2$ scavenger (28). DPBF possesses a strong absorption band centered at 418 nm. As depicted in *SI Appendix*, Fig. S22, for the mixed solution of **1** and DPBF, the intensity of the absorption band centered at 418 nm exhibits a continuous decrease under prolonged light irradiation, indicating $^1O_2$ formation by excitation of **1** that decomposes the DPBF. The Φ_Δ of **1** was calculated to be 88% using $[Ru(bpy)_3]^{2+}$ as a reference. This result is in good agreement with the direct method. The Φ_Δ of **1** is considerably higher than many organic and organometallic compounds including $[Ru(bpy)_3]^{2+}$ (14, 15, 27), presumably due to the enhanced intersystem crossing process by introduction of Pt (21, 22). The molecular ability to initiate the PDT process following two-photon excitation is often evaluated using a merit parameter $\sigma_2 \times \Phi_\Delta$ (29). The $\sigma_2 \times \Phi_\Delta$ value of 1,220 GM in **1** is much larger than that of tetraphenylporphyrin (1.5 GM) (29), revealing that **1** is a highly efficient two-photon $^1O_2$ sensitizer.

Cellular Uptake, Localization, and Imaging. The stability of complex **1** in aqueous media was assessed by monitoring the UV-Vis absorption spectrum at acidic (pH = 5) and physiological pH (pH = 7.4) conditions (*SI Appendix*, Fig. S23). In both conditions, less than 5% decrease in the absorbance was observed after 24 h, suggesting that **1** has a good stability.

The lipophilicity/hydrophilicity of a compound can significantly influence its cellular uptake and accumulation (24, 30). The octanol/water partition coefficient (log $P_{o/w}$) of **1** was determined to be −0.45, less hydrophilic than $[Ru(bpy)_3]^{2+}$ (log $P_{o/w}$ = −1.26) (*SI Appendix*, Fig. S24) due to the use of the hydrophobic bis(phosphine) Pt(II) building block. The lower hydrophilicity of **1** may facilitate its cell uptake efficiency and its selective localization.

Cellular localization of metallacycle **1** was examined using confocal laser scanning microscopy on human pulmonary carcinoma cell line A549. As shown in Fig. 3, **1** can enter cells and display strong deep-red intracellular luminescence under one-photon excitation. Colocalization studies of **1** with commercial lysosome dye LysoTracker Green (LTG), nuclear dye Hoechst 33342 (Hoechst), and mitochondrial dye MitoTracker Deep Red (MTDR) were performed in A549 cells (Fig. 3). The luminescence signal of **1** exhibited a good superimposition pattern with MTDR, with a correlation coefficient of 0.80, while a smaller amount of **1** is found to overlap with Hoechst, resulting in a lower correlation coefficient of 0.33. A weak correlation coefficient was found for LTG. This result indicates that **1** selectively localizes in mitochondria and nuclei.

The cellular uptake and the biodistribution of **1** were further quantified using inductively coupled plasma MS (ICP-MS) analysis. Time-dependent ICP-MS studies found that the total cellular

Table 1. ICP-MS quantification of the internalized Ru and Pt by A549 cells incubated with 1 for 2 h

Metal	Distribution in cytoplasm, %	Distribution in mitochondria, %	Distribution in nuclei, %
Ru	74.8	66.9	25.2
Pt	74.7	66.8	25.3

uptake of **1** reached a maximum after 12 h of incubation, with a concentration of 114.82 ng and 451.37 ng per million cells for Ru and Pt, respectively (*SI Appendix*, Fig. S25*A*). For precursor **2** under the same condition, a maximum cellular Ru concentration is recorded at 2.32 ng per million cells (*SI Appendix*, Fig. S26*A*), suggesting that macrocyclic assembly **1** has more favorable cellular uptake properties compared with its small-molecule precursor **2**. As for the subcellular distribution of **1**, 67% of both Ru and Pt contents were found in the mitochondria, whereas a smaller proportion entered the nuclei, where 25% of the intracellular Ru and Pt were found after incubation with **1** for 2 h in the dark (5 μM) (Table 1). Notably, it was calculated that the molar ratio of Ru:Pt is ∼1:2 in cells and within various organelles throughout the experiments on **1**, consistent with its stoichiometry. Due to the distinct cellular uptake and subcellular distribution behavior of **1** and the precursors (*SI Appendix*, Figs. S25–S27), these results provide evidence for the uptake and localization of **1** as an intact metallacycle.

Subcellular distribution is an important factor determining the efficacy of a PDT agent due to the short lifetime and limited diffusion range of ROS (31). Previous studies have shown that lipophilic, charged metal complexes may accumulate in the mitochondria because of the negative potential difference across the mitochondrial membrane (16, 24, 28). The introduction of tetramethylammonium-decorated Pt(II) acceptor **3** endows the metallacycle with a +10 charge and enhanced lipophilicity compared with small-molecule Ru(II) polypyridyl compounds, which may lead to the accumulation in mitochondria. Mitochondria are crucial regulators of the intrinsic pathway of apoptosis and multiple forms of nonapoptotic cell death (16). Elevated intracellular ROS levels within mitochondria can trigger caspase activation and apoptosis (32). Furthermore, mitochondria-targeting drugs interfere with mitochondrial redox functions and can induce mitochondrial-dependent cell death signaling pathway (16). Hence, the accumulation of **1** in mitochondria is favorable for its application as a PDT agent. In addition to mitochondria, **1** is also found to partly accumulate in the nucleus, presumably due to its large planar structure and overall positive charge that facilitates its interactions with DNA (33). The nucleus is also an effective subcellular target for PDT treatment because ROS produced in the nucleus can directly damage intranuclear DNA and inhibit DNA repair processes (25, 34). Furthermore, ROS generated in mitochondria and the nucleus induce cellular damage in different pathways, which could produce a synergistic effect, thus realizing a more efficient PDT treatment regimen. The dual mode of action of **1** may also minimize the potential resistance to PDT (35).

To determine the mechanism for the internalization of **1**, cellular uptake studies were conducted under lowered temperature or in the presence of metabolic and endocytic inhibitors (*SI Appendix*, Fig. S28). The energy dependency of cellular uptake of **1** was confirmed by a dramatic decrease in the uptake of **1** by A549 cells at lower temperature or pretreated with metabolic inhibitors 2-deoxy-D-glucose and oligomycin. Incubation of cells with an organic cation transporter inhibitor triethylamine did not influence the internalization of **1**, suggesting the uptake of **1** does not rely on active transport. Pretreatment of endocytic inhibitor NH_4Cl resulted in a decrease in intracellular luminescence intensity compared with the control, indicating that **1** internalizes into cancer cells by an energy-dependent endocytosis pathway.

Photoexcitation-Induced $^1O_2$ Generation and (Photo)Cytotoxicity in Cells. The cytotoxicity of **1** in the dark was investigated on various cancer cell lines, including HeLa, human pulmonary carcinoma cell line A549, cisplatin-resistant cell line A549R, multidrug-resistant human oral floor carcinoma cell line KV, and human prostate cancer cell line PC-3 using a 3-(4′,5′-dimethylthiazol-2′-yl)-2,5-diphenyl tetrazolium bromide assay. **1** was found to be weakly toxic toward the cells lines with IC_{50} values of 65.2–80.9 μM (*SI Appendix*, Table S1) in the dark. When exposed to light (450 nm, 21.8 mW/cm^2, 5 min), **1** had a significant influence on cell viability with IC_{50} values of 0.71–4.4 μM (*SI Appendix*, Table S1), resulting photocytotoxicity index (PI) [PI = $IC_{50(dark)}$/$IC_{50(light)}$] values of 11.6–114 (Table 2). Among the selected cells lines, A549 cells displayed the lowest IC_{50} value of 0.71 μM and 114-fold enhancement in cytotoxicity when irradiated. As a result, A549 cells were employed as the model cell line for the following studies. Cisplatin was employed as the positive control of the procedure, and its PI values were found to be ∼1 for all cells lines due to its low photosensitization activity. Notably, under the same conditions, **1** exhibited remarkably higher photocytotoxicity and PI values on all selected cell lines compared with cisplatin, $Ru(bpy)_3^{2+}$ and clinically approved PDT agent 5-aminolevulinic acid (5-ALA) (Table 2). In addition, the PI values for **1** are comparable to or even better than those of many Ru(II) polypyridyl photosensitizers under comparable experimental conditions (14, 15).

To demonstrate the capability of **1** to generate $^1O_2$ in vitro with two-photon irradiation, 2,7-dichlorodihydrofluorescein diacetate (DCFH-DA) was employed as an intracellular ROS indicator, which rapidly oxidized to yield highly fluorescent 2′,7′-dichlorofluorescein in the presence of ROS (36). A549 cells were incubated with **1** and DCFH-DA, and the confocal fluorescence images of the cells before and after two-photon light exposure were recorded. As illustrated in *SI Appendix*, Fig. S29, the morphology of the cells remained unchanged, and no fluorescence was observed before light exposure, suggesting low cytotoxicity of **1**. Marked green fluorescence was observed following two-photon light irradiation, indicating that **1** is an efficient two-photon photosensitizer in cells. The two-photon light used for photoexcitation is safe for the cells, as cells treated with only DCFH-DA exhibited normal morphology and no fluorescence enhancement after irradiation.

The ability of **1** act as a two-photon PDT agent was confirmed by calcein AM/ethidium homodimer-1 (EthD-1) costaining assay (*SI Appendix*, Fig. S30). Nonemissive calcein AM can be converted to green-emitting calcein by intracellular esterases in living cells, whereas EthD-1 can only enter cells with damaged membranes and emit red fluorescence upon binding to nucleic acids (37). A549 cells incubated with **1** in the dark displayed intense green fluorescence, implying most of the cancer cells were alive. Parts of the cells were then subjected to two-photon light irradiation, and cell death was found in the region irradiated, as evidenced by the loss of green fluorescence and the appearance of red fluorescence in the region. Moreover, cell shrinkage observed in the irradiated area indicated that severe cell damage occurred upon photoexcitation of **1**. To further assess the two-photon PDT efficacy of **1**, an annexin V-FITC/propidium iodide assay was performed (38) (*SI Appendix*, Fig. S31). After two-photon irradiation, both green staining (FITC)

Table 2. PI values for 1, 5-ALA, $Ru(bpy)_3^{2+}$ and cisplatin toward various cancer cell lines

Compound	A549	A549R	HeLa	KV	PC-3
1	114	64.3	20.7	11.6	14.8
5-ALA	>1.7	>1.37	>1.1	>1.1	n.d.
$Ru(bpy)_3^{2+}$	3.4	3.2	3.4	2.4	2.1
Cisplatin	0.97	0.97	1.0	1.0	1.0

n.d., not determined.

CHEMISTRY

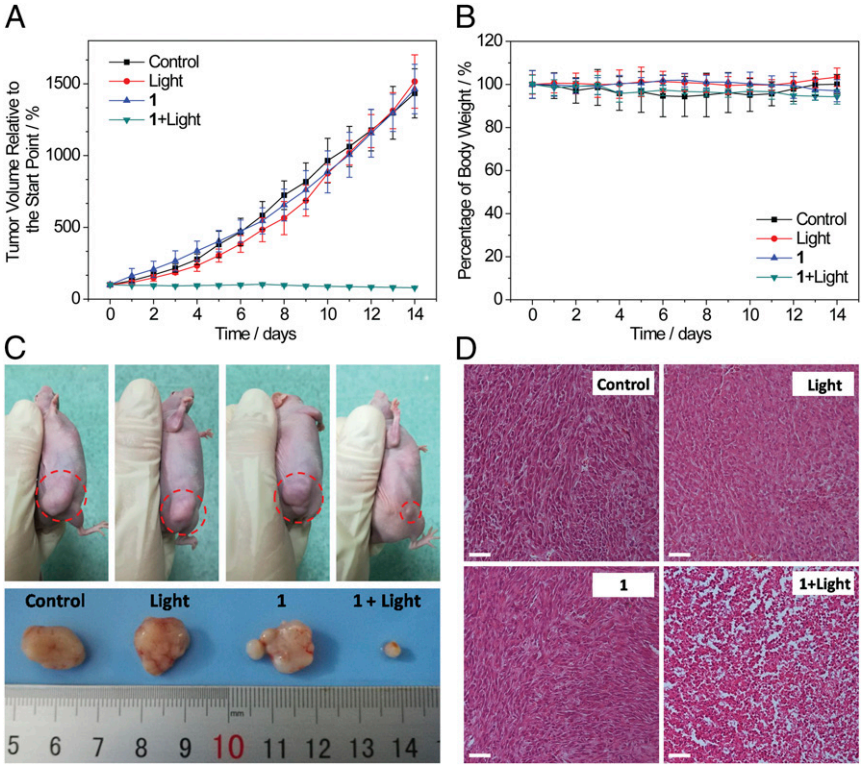

Fig. 4. Two-photon PDT in vivo. The mice were randomly allocated into four different treatments: (*i*) physiological saline (control), (*ii*) physiological saline and two-photon laser irradiation (light), (*iii*) **1**-injected only (**1**), and (*iv*) **1**-injected and subjected to two-photon laser irradiation (**1** + Light). (*A*) In vivo tumor growth inhibition curves for mice with four different treatments. (*B*) Average body weights of tumor-bearing mice with four different treatments. (*C*) Representative photographs of A549 tumors in mice with four different treatments. (*D*) Histological examination of tumors with four treatments after PDT. (Scale bars: 50 μm.)

on the cell surface and red staining (propidium iodide) throughout the nucleus were observed, indicating that the cells were in necrosis or late apoptosis.

The mechanism of cell death by photoexcitation of **1** was examined by measuring cellular caspase-3/7 activity via a luminescent assay (*SI Appendix*, Fig. S32). Caspases-3/7 are known for their central role in the execution of apoptosis in mammalian cells (39). In the absence of light, no enhancement in cellular caspase-3/7 activity was found for cells incubated with **1** compared with untreated cells, while increased caspase activity was detected in cells treated with cisplatin, in agreement with the cytotoxicity studies that show that **1** possesses weak toxicity. Upon light irradiation, cells incubated with **1** displayed a substantially higher caspase-3/7 activity relative to the untreated cells or cells treated with cisplatin, suggesting that PDT treatment with **1** effectively induce cellular apoptosis.

Since the majority of **1** accumulates in mitochondria, we investigated whether the mitochondria were damaged during the PDT treatment. Mitochondrial dysfunction was determined by measuring the changes in the mitochondrial membrane potential (MMP) before and after two-photon light irradiation with 5,5′,6,6′-tetrachloro-1,1′-3,3′-tetraethyl-benzimidazolylcarbocyanine iodide (JC-1). JC-1 is a mitochondria-selective dye that emits red fluorescence at high MMP and a green fluorescence at low MMP (40). As shown in *SI Appendix*, Fig. S33, cells treated with **1** displayed a distinct green emission after light irradiation, indicating loss of MMP and hence mitochondrial dysfunction compared with the untreated group, suggesting that **1** can induce cell apoptosis via mitochondria-mediated pathways.

The impact of the two-photon PDT on intranuclear DNA is examined using a TUNEL assay. After exposure to two-photon light irradiation, DNA fragmentation in the nuclei is observed for cells pretreated with **1** (*SI Appendix*, Fig. S34), indicating that the photoexcitation of **1** also lead to intranuclear DNA damage.

Two-Photon PDT in Vivo. The in vivo two-photon PDT efficacy of **1** was further evaluated using A549 tumor-bearing nude mice with a xenograft tumor volume of 80 mm^3. The mice were randomly allocated into four groups (five mice per group) before the experiments (day 0): physiological saline as control (group 1), physiological saline and two-photon laser irradiation (group 2), **1**-injected only (group 3), and **1**-injected and subjected to two-photon laser irradiation (group 4). The mice in group 4 were intratumorally injected with metallacycle **1** (0.5 mg/kg body weight). Two hours after the injection, the A549 tumor was irradiated with a diode laser (800 nm, 50 mW, 20 s/mm). The same laser dose and the same dose of **1** were employed in groups 2 and 3. On day 7, mice in group 2 and 4 were subjected to a second course of light irradiation at the same light dose used previously. The tumor volume and the body weight of the mice from each group were measured daily for 14 d. As shown in Fig. 4*A*, for the treatment group, the tumors shrank gradually, and were reduced to 78% of the original size in day 14, while the tumors in other groups showed more than 13-fold growth over the same period. No noticeable body weight loss was found during the treatment process (Fig. 4*B*), indicating the low level of side effects of the treatment. After PDT treatment, a histological examination was conducted on the tumors using H&E stain. The tumor tissues from group 4 displayed irreversible pathological alterations and degradation, suggesting necrosis or apoptosis of the tumor cells, whereas the tumor tissues from the other groups were composed of normal, tightly packed tumor cells (Fig. 4*D*). The system toxicity of the treatment was further examined by examination of the histology of the organs including the liver, kidney, spleen, heart, lung, brain, intestine, and ovary using H&E stain

(*SI Appendix*, Fig. S35). Neither irreversible pathological alterations nor injuries in the organs of mice of all four groups could be found, indicating low systemic toxicity of **1**. Therefore, the metallacycle **1** is favorable for in vivo PDT treatment of cancer with high efficacy and negligible toxicity to the healthy organs of the treated mice.

Conclusion

In summary, we prepared a heterometallic Ru–Pt metallacycle as a highly potent two-photon PDT agent via coordination-driven self-assembly. Formation of the metallacycle enables the interaction between the Ru(II) polypyridyl moiety and the Pt(II) metal center, which endows the ensemble with near-infrared emission, strong TPA, and high $^1O_2$ generation efficiency. The highly charged, large macrocyclic structure of the metallacycle facilitates its internalization in cells and dual localization in mitochondria and nuclei. The metallacycle exhibits weak cytotoxicity in the dark, and intracellular $^1O_2$ generated upon photoexcitation of the metallacycle induces cell death by simultaneously damaging mitochondria and nuclei, resulting in its high photocytotoxicity. In vivo investigations demonstrated that **1** efficiently ablates cancer tissues at low light doses with minimal system toxicity. We anticipate a promising future of this metallacycle as an agent for efficient and safe two-photon PDT. The facile tunability of coordination-driven self-assembly provides the possibility for future development of SCC-based PDT agents with intriguing properties, such as cell-specific uptake, overcoming the effects of hypoxia, and combination with other therapeutic modalities (e.g., radiotherapy, photothermal therapy, and chemotherapy). Furthermore, the supramolecular approach in tuning the properties of the Ru(II) polypyridyl complexes present herein may be of broad interest due to its diverse applications (41, 42).

Materials and Methods

All reagents and kits were commercially available and used as supplied without further purification. All experimental protocols involving live animals were approved by the Sun Yat-sen University Animal Care and Use Committee. The details of the materials, methods including synthesis and characterization of compounds, and in vitro and in vivo two-photon PDT studies on metallacycle **1** are described in *SI Appendix*.

ACKNOWLEDGMENTS. This work was supported by NIH Grant R01 CA215157 (to P.J.S.), National Science Foundation of China Grants 21525105, 21471164, and 21778079 and 973 Programs Grant 2015CB856301 (to H.C.), and National Science Foundation Grant CHE-1506722 (to X.L.).

1. Chakrabarty R, Mukherjee PS, Stang PJ (2011) Supramolecular coordination: Self-assembly of finite two- and three-dimensional ensembles. *Chem Rev* 111:6810–6918.
2. Harris K, Fujita D, Fujita M (2013) Giant hollow M(n)L(2n) spherical complexes: Structure, functionalisation and applications. *Chem Commun (Camb)* 49:6703–6712.
3. Lifschitz AM, Rosen MS, McGuirk CM, Mirkin CA (2015) Allosteric supramolecular coordination constructs. *J Am Chem Soc* 137:7252–7261.
4. Therrien B (2012) Drug delivery by water-soluble organometallic cages. *Top Curr Chem* 319:35–55.
5. Zheng Y-R, Suntharalingam K, Johnstone TC, Lippard SJ (2015) Encapsulation of Pt(IV) prodrugs within a Pt(II) cage for drug delivery. *Chem Sci (Camb)* 6:1189–1193.
6. Ronson TK, Meng W, Nitschke JR (2017) Design principles for the optimization of guest binding in aromatic-paneled $Fe^{II}_4L_6$ cages. *J Am Chem Soc* 139:9698–9707.
7. Kaphan DM, Levin MD, Bergman RG, Raymond KN, Toste FD (2015) A supramolecular microenvironment strategy for transition metal catalysis. *Science* 350:1235–1238.
8. Wang Q-Q, et al. (2016) Self-assembled nanospheres with multiple endohedral binding sites pre-organize catalysts and substrates for highly efficient reactions. *Nat Chem* 8:225–230.
9. Yan X, Cook TR, Wang P, Huang F, Stang PJ (2015) Highly emissive platinum(II) metallacages. *Nat Chem* 7:342–348.
10. Walker MG, et al. (2016) A self-assembled metallomacrocycle singlet oxygen sensitizer for photodynamic therapy. *Chemistry* 22:5996–6000.
11. Garci A, et al. (2017) Efficient and rapid mechanochemical assembly of platinum(II) squares for guanine quadruplex targeting. *J Am Chem Soc* 139:16913–16922.
12. Ahmad H, Hazel BW, Meijer AJHM, Thomas JA, Wilkinson KA (2013) A self-assembled luminescent host that selectively senses ATP in water. *Chemistry* 19:5081–5087.
13. Ng KK, Zheng G (2015) Molecular interactions in organic nanoparticles for phototheranostic applications. *Chem Rev* 115:11012–11042.
14. Heinemann F, Karges J, Gasser G (2017) Critical overview of the use of Ru(II) polypyridyl complexes as photosensitizers in one-photon and two-photon photodynamic therapy. *Acc Chem Res* 50:2727–2736.
15. Liu J, et al. (2018) Harnessing ruthenium(II) as photodynamic agents: Encouraging advances in cancer therapy. *Coord Chem Rev* 363:17–28.
16. Fulda S, Galluzzi L, Kroemer G (2010) Targeting mitochondria for cancer therapy. *Nat Rev Drug Discov* 9:447–464.
17. Saeed HK, et al. (2017) Homo- and heteroleptic phototoxic dinuclear metallo-intercalators based on Ru^{II} (dppn) intercalating moieties: Synthesis, optical, and biological studies. *Angew Chem Int Ed Engl* 56:12628–12633.
18. White JK, Schmehl RH, Turro C (2017) An overview of photosubstitution reactions of Ru(II) imine complexes and their application in photobiology and photodynamic therapy. *Inorg Chim Acta* 454:7–20.
19. Pollock JB, Cook TR, Stang PJ (2012) Photophysical and computational investigations of bis(phosphine) organoplatinum(II) metallacycles. *J Am Chem Soc* 134:10607–10620.
20. Shi P, et al. (2015) Uniting ruthenium(II) and platinum(II) polypyridine centers in heteropolymetallic complexes giving strong two-photon absorption. *Inorg Chem* 54:11450–11456.
21. Lu K, He C, Lin W (2014) Nanoscale metal-organic framework for highly effective photodynamic therapy of resistant head and neck cancer. *J Am Chem Soc* 136:16712–16715.
22. Zhang Y, et al. (2017) Photophysical enhancement of triplet emitters by coordination-driven self-assembly. *Chemistry* 23:4532–4536.
23. Medishetty R, et al. (2017) Multi-photon absorption in metal-organic frameworks. *Angew Chem Int Ed Engl* 56:14743–14748.
24. Puckett CA, Ernst RJ, Barton JK (2010) Exploring the cellular accumulation of metal complexes. *Dalton Trans* 39:1159–1170.
25. Pan L, Liu J, Shi J (2014) Intranuclear photosensitizer delivery and photosensitization for enhanced photodynamic therapy with ultralow irradiance. *Adv Funct Mater* 24:7318–7327.
26. Velusamy M, et al. (2009) A new series of quadrupolar type two-photon absorption chromophores bearing 11, 12-dibutoxydibenzo[a,c]-phenazine bridged amines; their applications in two-photon fluorescence imaging and two-photon photodynamic therapy. *Adv Funct Mater* 19:2388–2397.
27. Bolze F, Jenni S, Sour A, Heitz V (2017) Molecular photosensitisers for two-photon photodynamic therapy. *Chem Commun (Camb)* 53:12857–12877.
28. Liu J, et al. (2015) Ruthenium(II) polypyridyl complexes as mitochondria-targeted two-photon photodynamic anticancer agents. *Biomaterials* 56:140–153.
29. Drobizhev M, et al. (2005) Extremely strong near-IR two-photon absorption in conjugated porphyrin dimers: Quantitative description with three-essential-states model. *J Phys Chem B* 109:7223–7236.
30. Puckett CA, Barton JK (2007) Methods to explore cellular uptake of ruthenium complexes. *J Am Chem Soc* 129:46–47.
31. Rosenkranz AA, Jans DA, Sobolev AS (2000) Targeted intracellular delivery of photosensitizers to enhance photodynamic efficiency. *Immunol Cell Biol* 78:452–464.
32. Ott M, Gogvadze V, Orrenius S, Zhivotovsky B (2007) Mitochondria, oxidative stress and cell death. *Apoptosis* 12:913–922.
33. Li G, Sun L, Ji L, Chao H (2016) Ruthenium(II) complexes with dppz: From molecular photoswitch to biological applications. *Dalton Trans* 45:13261–13276.
34. Yu Z, Pan W, Li N, Tang B (2016) A nuclear targeted dual-photosensitizer for drug-resistant cancer therapy with NIR activated multiple ROS. *Chem Sci* 7:4237–4244.
35. Casas A, Di Venosa G, Hasan T, Al Batlle (2011) Mechanisms of resistance to photodynamic therapy. *Curr Med Chem* 18:2486–2515.
36. Kalyanaraman B, et al. (2012) Measuring reactive oxygen and nitrogen species with fluorescent probes: Challenges and limitations. *Free Radic Biol Med* 52:1–6.
37. King MA (2000) Detection of dead cells and measurement of cell killing by flow cytometry. *J Immunol Methods* 243:155–166.
38. Casciola-Rosen L, Rosen A, Petri M, Schlissel M (1996) Surface blebs on apoptotic cells are sites of enhanced procoagulant activity: Implications for coagulation events and antigenic spread in systemic lupus erythematosus. *Proc Natl Acad Sci USA* 93:1624–1629.
39. Walsh JG, et al. (2008) Executioner caspase-3 and caspase-7 are functionally distinct proteases. *Proc Natl Acad Sci USA* 105:12815–12819.
40. Smiley ST, et al. (1991) Intracellular heterogeneity in mitochondrial membrane potentials revealed by a J-aggregate-forming lipophilic cation JC-1. *Proc Natl Acad Sci USA* 88:3671–3675.
41. Kunz V, et al. (2017) Cooperative water oxidation catalysis in a series of trinuclear metallosupramolecular ruthenium macrocycles. *Energy Environ Sci* 10:2137–2153.
42. Notaro A, Gasser G (2017) Monomeric and dimeric coordinatively saturated and substitutionally inert Ru(II) polypyridyl complexes as anticancer drug candidates. *Chem Soc Rev* 46:7317–7337.